Erosion and Erosion-Corrosion Performance of Cast and Thermally Sprayed Nickel-Aluminium Bronze

R.C. Barik[1], J.A. Wharton[1], R.J.K. Wood[1], K S Tan[2] and K.R. Stokes[3]

[1]Materials Research Group, School of Engineering Sciences,
University of Southampton, Highfield, Southampton, SO17 1BJ, UK

[2]Max Planck Institut fuer Eisenforschung, GmbH,
Max-Planck-Straße 1, 40237 Düsseldorf, Germany

[3]Physical Sciences Department, Dstl Porton Down,
Salisbury, Wiltshire, SP4 0JQ, UK

krstokes@dstl.gov.uk

ABSTRACT

Nickel-Aluminium Bronze (NAB) is widely used for propulsion and seawater handling systems in naval platforms. It is selected because of its attractive combination of toughness and shock resistance but it has inherent susceptibility to selective phase corrosion and erosion-corrosion. In order to extend the life of NAB components, modern coating techniques are being considered in order to confer improved wear and corrosion resistance, as well as a method of providing cost effective refurbishment. This paper presents research into erosion and erosion-corrosion of both ''as cast'' and thermally sprayed NAB. The synergistic effects based on mass loss measurements obtained from pure erosion (E), flow corrosion (C) and erosion-corrosion (T) experiments are presented under a range of energies that relate to maritime operating conditions. The influence of synergy was found to be dependent on flow energy and could be either beneficial or detrimental. The results of this work assist with material selection for controlled or reduced material loss in marine vessels.

1.0 INTRODUCTION

1.1 Background

Seawater is used for fire-fighting and cooling systems, not only in naval vessels but also within oil and gas production, power generating industries and commercial shipping. However, sand particles can be entrained in the seawater, which reduce the design life by a combination of erosion and corrosion. If erosion and corrosion attack occurs simultaneously, this can enhance the overall material wastage through a synergistic effect due to a coupling between erosion, a mechanical process, and the electrochemical process of corrosion.

In the case of naval platforms, nickel-aluminium bronzes (NAB) are widely used for propulsion and seawater handling systems. These alloys contain typically 9-12% Al with additions of up to 6% each of Fe and Ni and possess high toughness and erosion-corrosion resistance characteristics along with good resistance to seawater corrosion by virtue of a stable and strongly adherent oxide film [1]. This protective film consists of two layers, an inner layer of cuprous oxide (Cu_2O) and an outer layer of alumina (Al_2O_3) [2]. Damage or depassivation of the surface film occurs by exposure to high velocities, cavitation and particle impingement, phenomena that can occur in both seawater and propulsion systems, although the ability of nickel-aluminium bronze to quickly repassivate can result in low corrosion rates; hence it's original selection for naval applications. Localised damage of this protective surface film, however, has

Paper presented at the RTO AVT Specialists' Meeting on "The Control and Reduction of Wear in Military Platforms", held in Williamsburg, USA, 7-9 June 2003, and published in RTO-MP-AVT-109.

Report Documentation Page

Form Approved
OMB No. 0704-0188

1. REPORT DATE	2. REPORT TYPE	3. DATES COVERED
01 JUN 2004	**N/A**	**-**

4. TITLE AND SUBTITLE	5a. CONTRACT NUMBER
Erosion and Erosion-Corrosion Performance of Cast and Thermally Sprayed Nickel-Aluminium Bronze	5b. GRANT NUMBER
	5c. PROGRAM ELEMENT NUMBER
6. AUTHOR(S)	5d. PROJECT NUMBER
	5e. TASK NUMBER
	5f. WORK UNIT NUMBER
7. PERFORMING ORGANIZATION NAME(S) AND ADDRESS(ES) **1Materials Research Group, School of Engineering Sciences, University of Southampton, Highfield, Southampton, SO17 1BJ, UK**	8. PERFORMING ORGANIZATION REPORT NUMBER
9. SPONSORING/MONITORING AGENCY NAME(S) AND ADDRESS(ES)	10. SPONSOR/MONITOR'S ACRONYM(S)
	11. SPONSOR/MONITOR'S REPORT NUMBER(S)

12. DISTRIBUTION/AVAILABILITY STATEMENT
Approved for public release, distribution unlimited

13. SUPPLEMENTARY NOTES
See also ADM201869, RTO-MP-AVT-109 The Control and Reduction of Wear in Military Platforms (Contrôle et réduction de lusure des plates-formes militaires)., The original document contains color images.

14. ABSTRACT

15. SUBJECT TERMS

16. SECURITY CLASSIFICATION OF:			17. LIMITATION OF ABSTRACT	18. NUMBER OF PAGES	19a. NAME OF RESPONSIBLE PERSON
a. REPORT	b. ABSTRACT	c. THIS PAGE			
unclassified	**unclassified**	**unclassified**	**UU**	**24**	

resulted in pitting and/or selective phase corrosion (SPC) a problem exacerbated by the entrainment of sand particles, as mentioned above. In addition cavitation erosion is a problem particularly associated with propulsion systems.

In order to improve the erosion-corrosion performance of NAB the use of coatings has been considered and, as an economic alternative to components made from high corrosion resistant alloys, the application of organic and metallic coatings systems to cheap substrates have also been investigated. A further advantage of applying coatings is that they provide a cost-effective approach for recovering components that are worn or corroded.

In this work, the use of the High Velocity Oxy-fuel (HVOF) technique was explored as a way of producing resistance to wear and erosion. Components that could potentially be coated using the HVOF method include propellers; pump impellers and casings, valve bodies/trim and pipe systems. Unfortunately, porosity introduced during the spraying process is a common phenomenon for all thermal coatings. Such porosity is detrimental towards the corrosion protection offered by the coating; electrolyte can permeate the coating reducing not only its own life but also that of the substrate. It is, therefore, desirable to fabricate coatings that can reduce or prevent corrosive electrolytes from reaching the substrate by forming insoluble corrosion products at the pores.

1.2 Synergy

All common metals and alloys rely on the formation of a superficial layer or film of oxide or other corrosion product to protect the underlying metal from further attack. Under service conditions involving exposure to liquids flowing at high speed, a shear stress at the metal surface can be generated which may damage this protective film, locally exposing unprotected bare metal. This is a form of wear which becomes more severe with a high degree of local turbulence or if the flow contains abrasive particles such as sand. The continued effect of erosion, preventing permanent formation of a protective film and the corrosion of bare metal consequently exposed, can lead to rapid local attack causing substantial metal loss and often penetration. This type of attack is known as erosion-corrosion or jet impingement [3]. The component of material loss under erosion–corrosion (T) is often represented by Equation (1).

$$T = E + C + S \qquad \ldots\ldots(1)$$

where E is the material loss by pure mechanical erosion processes, C is the material loss by electrochemical corrosion processes and S ,the synergy, is the combined interaction between erosion and corrosion process.

Thus, synergy is defined as “the difference between erosion-corrosion and the sum of its two parts” and can be expressed by Equations (2) and (3).

$$S = T - (E + C). \qquad \ldots\ldots(2)$$

Synergy can be broken down into two components, ΔE and ΔC, where ΔE is the corrosion-enhanced erosion and ΔC is the erosion-enhanced corrosion, see Equation (3) [4].

$$S = \Delta E + \Delta C. \qquad \ldots\ldots(3)$$

Erosion can mechanically strip the protective corrosion film creating fresh reactive corrosion sites and producing ΔC [5], dependent on the rate of repassivation and the integrity of the film formed. Other possible erosion-enhanced corrosion mechanisms include (*i*) local acidification at erosion sites, accelerating corrosion rates and prohibiting film formation, (*ii*) increased mass transport by high turbulence levels, (*iii*) lowering the fatigue strength of a metal by corrosion and (*iv*) surface roughening of

the specimen during particle impact enhanced mass transfer effects increased the corrosion rate [6]. Corrosion-enhanced erosion mechanisms are also possible (ΔE). The ΔE wear rate could be due to (*v*) the removal of work hardened surfaces by corrosion processes which expose the underlying base metal to erosion mechanisms [7], (*v*) preferential corrosive attack at grain boundaries resulting in grain loosening and eventual removal [8], (*vii*) the increase in the number of stress concentration defects resulting from micropitting and (*viii*) detachment of plastically deformed flakes on the metal surface due to stress corrosion cracking. Most of the above mechanisms, if dominant, would be expected to lead to positive synergy. However, in some instances negative synergy can occur. Possible mechanisms that reduce erosion rates (-ΔE) are (*ix*) increased work hardening due to corrosion mechanisms, (*x*) shot-peening [9] by high velocity sand particle impacts or (*xi*) the presence of a soft or loosely adherent corrosion film or (*xii*) blunting of the crack tips by lateral dissolution retarding the speed of crack propagation. The reduction in corrosion rates (-ΔC) could result from rapid corrosion film growth, scaling or the formation of a passive film reducing corrosion rates dramatically.

1.3 Erosion-corrosion of protective coatings

Many investigations have covered the erosion-corrosion behaviour of metallic and polymeric based protective coatings [e.g. 13-16]. In general, plastic deformation was observed for ductile coatings, while brittle coatings eroded by cracking and chipping mechanisms. Coatings usually consist of both ductile and brittle constituents and the erosion behaviour is dominated by the major component. When a particular coating is exposed to abrasive particles in a corrosive medium, mass transfer effects between the coating/liquid and the substrate/liquid can affect the slurry erosion-corrosion behaviour of the coating due to increased oxide formation. At the same time, porosity introduced during the coating process will allow the liquid to permeate through the coating leading to possible galvanic corrosion between the coating and substrate, thus accelerating the material wastage during erosion.

Bardal *et al*. [13,14] carried out erosion-corrosion tests on a range of metallic and cermet coatings, produced by a range of coating processes (chemical vapour deposition, thermal spray and HVOF). Erosion, flow corrosion and erosion-corrosion experiments were carried out using a rotating disc apparatus, in synthetic seawater. Corrosion of the metallic binder in the cermet coatings undermined the carbide particles, leading to enhanced material loss. HVOF Ni-Cr-Si-B-C coatings subjected to erosion-corrosion in 3.5 % NaCl solution, using a submerged jet impingement rig, resulted in surface roughening mechanism due to erosion, followed by corrosion of less noble coating constituents. This lead to removal of 'unsupported protruding materials' by further sand particle impingement. Microscopy revealed that selective corrosion at the splat boundaries resulted in dislodgement of splat particle by erosion. Similarly, tests on HVOF WC-Co-Cr coatings reported by Perry *et al*. [17] showed that preferential corrosion occurred at the metallic binder followed by removal of the hard carbides by sand particle impingement.

This investigation aims to study the behaviour of cast nickel-aluminium bronze and HVOF nickel aluminium bronze coatings under erosion, corrosion and erosion-corrosion conditions. Quantification of only synergistic effects will be presented based on mass loss measurements obtained from pure erosion, flow corrosion and erosion-corrosion.

2 TEST MATERIALS

The chemical compositions of cast NAB (UNS C95800), HVOF aluminium bronze (AB) coating, HVOF NAB coating and BS 4360 steel used in the current investigations are shown in Table 1, in addition the material properties are shown in Table 2.

Cast NAB:- The microstructural analysis carried out on cast NAB after etching with 10%wt $FeCl_3$ in methanol reveals various α, β and κ-phases, see Figure 1 [19]. The light etched area in Figure 1 is the α-

phase while the large dendritic-shaped particle is κ_I precipitate. The κ_{II} precipitates are the smaller dendritic-shaped particles many of which are unevenly distributed at the α/β boundaries. The κ_{III} precipitates are lamellar or globular eutectoid decomposition products. The small precipitates distributed throughout the α-phase are κ_{IV} precipitates. The very dark-etched areas are the retained β-phase, otherwise called the martensitic β-phase.

HVOF NAB coating:- The coating was deposited on a BS 4360 steel substrate using a commercial Diamond Jet HVOF spraying system by the Centre of Thermal Spray Technology, University of Barcelona. The NAB coating was formulated from three types of commercially available HVOF powders. Final coating composition is given in Table 1 based on copper, nickel and iron. Figure 2(a) shows a SEM transverse section of the as-sprayed NAB coating with a coating thickness nominally 300 μm. The coating was built up by semi-molten splats, spreading up to 80 μm in the horizontal direction. Unmelted particles were observed in the transverse section. The coating/substrate interface was well-bonded, with alumina grit blast remnants present at the interface. The NAB coating has a heterogeneous appearance, consisting of the different types of HVOF powders, EDX spectra obtained from the lighter phases revealed that it consists of aluminium bronze particles. Darker phases were found to be stainless steel particles and Ni5Al alloy particles.

HVOF AB Coating:- The AB coating was deposited onto the steel substrate using a Diamond Jet HVOF spray gun system by Sulzer Metco (UK) and the coating thickness was 230-250 μm, see Figure 2(b). The high amounts of copper in the partially molten and fully molten splat particles were distributed throughout the coating. Splat sizes were typically 50 μm. Numerous pores, ranging in size from 0.1 to 1 μm, are also clearly present throughout the coating.

Specimen Preparation:- The specimens used in the erosion and erosion-corrosion experiments were ground (up to grade 1200 SiC paper) and lapped (up to 3 μm diamond suspension) to a surface finish of R_a < 1 μm. Before and after each test, specimens were washed in water and degreased with acetone, dried in a jet of cold air and then weighed by a precision balance with a range of 205 g and accuracy of ±0.02 mg after 2 days in a dessicator to obtain mass loss results.

3 EXPERIMENTAL PROCEDURE

The tests were carried out using a slurry jet impingement rig, previously described in detail [17,20-22], for a range of kinetic energies from 0.02 to 0.40 μJ. Modifications have been made to accommodate a silver/silver chloride (Ag/AgCl) reference electrode (RE) and a platinum counter electrode (CE), see Figure 3. The ejector assembly, used for sand particle intake, was located downstream to prevent erosion damage on the counter and reference electrodes. A valve situated near the ejector allowed the sand intake to be completely isolated under flow corrosion conditions. The flow corrosion test electrolyte consisted of a 3.5 % NaCl solution, while the slurry was a 3.5 % NaCl solution with a 3% w/w silica sand concentration. Pure corrosion (C) experiments were carried out in the absence of slurry, whilst the erosion-corrosion (T) experiments were carried out with sand. Gamry PC4-750 potentiostat and ESA400 software were used to monitor the potential. For pure erosion (E), a -200 mV cathodic protection was applied based on the potentials observed from erosion-corrosion conditions. The test duration was 5 hours. A full summary of the experimental conditions are listed in Table 3.

4 RESULTS AND DISCUSSION

4.1 Gravimetric Mass Loss Measurements

The mass loss rate (mg/hour) between flow corrosion, pure erosion and erosion-corrosion for the cast NAB, the HVOF NAB coating and 4360 steel (as a reference material) are shown in Table 4 and Figures

4-6, respectively. Thus, direct comparisons can be made between the different test conditions; however this does assume that C, E, and T occurred uniformly over the specimen surface. The flow corrosion rates for cast NAB, NAB coating and steel are relatively constant, whereas for the E and T test conditions there is increasing material loss which can be attributed to the increase in erodent kinetic energy (E_k). Higher E_k will produce greater plastic deformation/cutting wear [22] and also for the T condition the freshly exposed metal will also result in higher corrosion rates depending on the repassivation characteristics.

4.2 Flow Corrosion Study

Figure 7 shows the flow corrosion rate (mm/year) for cast NAB, HVOF NAB and the 4360 steel for the different jet velocities. An additional result for an AB coating has also been included for comparison. The relatively high and uniform corrosion rate for the steel is consistent with a non-passivating metal. The formation of loosely adherent corrosion products will be immediately removed by the impinging jet exposing fresh surfaces allowing corrosion to continue at a uniform rate. Conversely, NAB is generally regarded as remaining passive under both static and a range of flow conditions [1]. The measured flow corrosion rates of cast NAB and the HVOF NAB coating at 0.5-0.8 and 0.8-1.5 ms^{-1}, respectively, are similar to those reported by Ault [10] for cast NAB alloys (i.e. 0.5-2.0 mm/year at 7.6 ms^{-1}). Corrosion rates of 0.015 mm/year are typically reported for NAB alloys under static conditions [1]. An SEM investigation of the cast NAB exposed to flow rates of 5 ms^{-1} was carried out near the centre of the specimen (see Figure 8) and this shows evidence of corrosion of the α-phase, see Figure 9(a). As described previously, the susceptible phases are anodic to the rest of the NAB microstructure due to higher aluminium contents and consequently undergo preferential corrosion [19]. Under flow conditions corrosion of these susceptible phases could occur before the formation of the protective film and it is considered that it would not form within the test duration. Alternatively, under jet impingement conditions it is considered that the shear stresses generated at the metal surface could be sufficient to either prevent initial formation or cause damage to the protective film [3]. The corrosion rate was shown to increase above a flow rate of 5 ms^{-1}.

The flow corrosion rate of HVOF NAB is higher than for the cast NAB. This is probably related to the discontinuous nature of the coating surface films caused by the pore structure and coating impurities. The HVOF NAB, see Figure 9(b), shows the development of a uniform corrosion film and also areas of discontinuity can be seen due to pore openings and local dissolution / pit sites.

4.3 Erosion Study

In addition to gravimetric mass loss measurement, erosion rates have been expressed as volume loss per impact (V_u) to allow for sand size variations at a given volume fraction:

$$V_u = \frac{M\pi d^3}{6\rho Q_v t C_v} \qquad \ldots\ldots(4)$$

where M is the mass loss, d is the mean sand diameter, ρ is the density Q_v is the slurry volume flow rate, C_v is the volume fraction of sand and t is the test duration.

The erosion rate V_u is related to the kinetic energy, E_k by

$$V_u \alpha (E_k)^l \qquad \ldots\ldots(5)$$

where l is the kinetic energy exponent. The kinetic energy E_k for erosion experiments is given by

$$E_k = 0.5mv^2 \qquad \ldots\ldots(6)$$

where m and v are the mean particle mass and velocity. The mean particle velocity within the slurry jet is assumed to be similar to the jet velocity.

Table 5 and Figure 10 show the relationship between kinetic energy, E_k, and erosion rates, V_u, under pure erosion conditions. The erosion rates for cast NAB, NAB coating, AB coating and steel generally increase with increasing kinetic energy, with the cast NAB giving superior erosion performance than the NAB coating. The erosion behaviour of the NAB coating has been reported to be dominated by cracking of splat boundary oxides [18]. This is due to the NAB coating having a heterogeneous microstructure consisting of particles from the different constituent alloy powders each of different mechanical properties, see Table 2. Kinetic energy exponents in Table 6 have been obtained for cast NAB, AB coating, NAB coating and 4360 steel. Ductile materials have energy exponent values close to unity while brittle materials have values in a range between 2 and 3 [23-25]. Ductile erosion mechanisms are kinetic energy related, whereas brittle materials are influenced by the presence of flaws which accelerate damage rates. The results from our tests show that cast NAB has an energy exponent close to unity consistent with a ductile material. In comparison, the NAB coating has a slightly higher kinetic energy exponent suggesting a combination of both ductile and brittle erosion mechanisms possibly due to the porosity within the NAB coating. Pores are considered to be made up of oxides that are formed during spraying and were found to be stress raisers under sand particle impingement [26-28].

The SEM analysis of the erosion scar surfaces, for both the cast NAB and NAB coating, can be seen in Figure 11. For the cast NAB, at the location of maximum erosion depth (Figure 11a) shows evidence of erodent particles producing overlapping impacts with plastic deformation. Whereas, the outer region of the erosion scar clearly reveals microcutting wear scars on the surface. The cutting marks are caused by the formation of plastic lips on the either side of the cutting mark. The cutting marks were associated with particles contacting the surface at an oblique angle, due to the hydrodynamic streamlines of the slurry jet. Similar erosion features are also evident on the HVOF NAB coating, in Figure 11(c and d), although the microcutting scars are less well-defined.

4.4 Erosion-Corrosion Study

The relationship between V_u and erodent kinetic energy under erosion-corrosion condition shows the material loss increased with kinetic energy, see Figure 12. At low energies the cast and HVOF NAB surfaces have similar resistances to erosion-corrosion. However, at higher energies the cast NAB always out-performs the HVOF NAB. For the cast NAB the kinetic energy exponents under erosion-corrosion conditions (l = 0.93) are slightly lower than the pure erosion conditions (l = 1.03), see Table 6. Similarly for the NAB coating, the kinetic energy exponents under erosion-corrosion conditions (l = 1.18) are slightly lower than pure erosion conditions (l = 1.21). The lower kinetic energy exponent is associated with the ability to form an adherent protective oxide film under corrosive conditions. This could result in a reduction in the wear rate, especially when the oxide layer remains intact under particle impingement (overall, the erosion-corrosion rate for HVOF NAB is higher compared with the cast NAB). The higher NAB coating wear rate at high kinetic energies could be due to cracking of brittle oxides that occur at the splat boundaries, thus the removal of whole splats can occur. Conversely, for the 4360 steel which is a non-passivating material the kinetic energy exponent under erosion-corrosion (l = 0.87) is higher than pure erosion conditions (l = 0.79). In this instance uniform corrosion, coupled with stress corrosion cracking of the work hardened plastic deformation lips contribute to an increased wear rate under erosion-corrosion conditions.

Figure 13 shows the SEM analysis of the erosion-corrosion scars for both the cast NAB and HVOF NAB coating. It is evident that compared with the erosion scars in Figure 11 the individual erosion-corrosion

impact scars are less clearly visible, i.e. the plastic deformation lips have been removed by corrosion or conversely corrosion has inhibited their formation. In the outer regions, there appears to be more corrosion activity with attack at the more active phases resulting in localised pitting and whole phase dissolution. This corrosion reveals the NAB microstructure that which could ultimately influence the phases exposed to erosion, for instance the relatively hard κ_I and κ_{IV}-phases. A tentative comparison of the HVOF NAB system under erosion and erosion-corrosion shows similar lack of lip features around impact scars and some evidence of partial slap removal, which is not seen for the cast NAB.

4.5 Synergy

In order to quantify the amount of the synergy, the synergy percentage (S/T %) for cast NAB, HVOF NAB coating and the steel can be plotted against erosion-corrosion rate V_u, see Figure 14. Negative synergy was found at all kinetic energies for cast NAB and this means there is an 'in-built' safety factor. Positive synergy was found for the HVOF NAB coating at high energy, suggesting a greater sensitivity to energy and/or increased corrosion activity. This is consistent with the HVOF NAB coating suffering additional damage mechanisms related to crack propagation at the splat boundary and/or splat ejection at high energy compared to those seen on the cast NAB. Negative synergy is beneficial and not all engineering surfaces demonstrate this property. However, it is the influence of the NAB coating microstructure that affects performance at high energy where the mixed mode of microcutting and splat removal allows increased corrosion resulting in a positive synergy.

Under erosion-corrosion conditions the majority of material loss usually results from mechanical damage as a result of erosion. Hence, when the rates of T and E are similar, as seen in Table 4, negative S values are obtained. This type of behaviour implies that the presence of corrosion films reduces the erosivity of the erodent. As revealed in the SEM analysis the outer regions of the scars typically had less evidence of microcutting. In addition, flow corrosion can also increase the difference between T and E+C values, resulting in negative synergy. This is especially true when substantially thick oxide film or corrosion products are formed on the flow corrosion and erosion-corrosion surfaces, affecting the mass loss measurements. For instance, this is most apparent for the steel at low kinetic energy where there is a significant negative synergy.

Table 7 compares the potential particle kinetic energies for a number of marine components, from pipe to a propulsor (assuming a particle diameter of 100 μm). It shows that for the experimental kinetic energies used in this study, cast NAB is suitable for most applications. Whereas, the HVOF NAB coating should only be considered for either pipework or valves due the poor performance at high kinetic energy. The coating has not been fully optimised, thus there is room for further improvements.

5 CONCLUSIONS

- For flow velocities between 3 to 5 ms^{-1} the corrosion rate of cast NAB is 0.5-0.6 mm/y demonstrating it is susceptible to flow corrosion, suggesting concerns for field applications. This is particularly reinforced for velocities above 5 ms^{-1} where the corrosion rate is enhanced. The corrosion rate under flow conditions were similar to those reported by Ault[10].
- Comparing the flow corrosion rates for the HVOF NAB coating to those of the steel substrate demonstrates that the coating offers 5x higher resistance than the uncoated substrate. However, the HVOF NAB coating is slightly inferior to the cast NAB under the flow conditions employed in this work.
- Under low kinetic energy cast NAB has good erosion-corrosion performance, but at a higher kinetic energy results infer a positive synergy and, hence, some vulnerability.

- The option of using HVOF NAB coatings for refurbishment of marine components is viable for low kinetic energy applications but further improvements in coating integrity are required before this option can be subjected to high energy.
- The HVOF NAB coating has a higher sensitivity to impact energy due to the high flaw density and splat boundaries, which act as crack initiators.
- Under erosion conditions and at low energy the HVOF NAB coating offers similar resistance to the cast alloy, with both eroding by the predominately ductile mechanisms of deformation and cutting wear. With increased energies the coating offers increasingly less resistance relative to the cast material due to crack propagation and splat ejection.
- Comparison of erosion performance with erosion-corrosion performance shows both coating and cast surfaces demonstrate a propensity for negative synergy, although potential vulnerability to positive synergy at high energies was seen for the coating. Negative synergies infer good properties under combined mechanical and electrochemical degradation.

6 REFERENCES

[1] A.H. Tuthill, Guidelines for the use of copper alloys in seawater, *Mater. Perform*., **26** (1987) 12-22.

[2] A. Schussler, H.E. Exner, The corrosion of nickel-aluminium bronzes in seawater - I. Protective layer formation and the passivation mechanism, *Corros. Sci*., **34** (1993) 1793-1802.

[3] H.J. Meigh, Cast and wrought aluminium bronzes properties, processes and structure, 1st edition 2000, IOM Communications Ltd., London, United Kingdom.

[4] KS Tan, JA Wharton, RJK Wood, Solid particle erosion-corrosion behaviour of a novel HVOF nickel aluminium bronze coating for marine applications – correlation between mass loss and electrochemical measurements, ICEAW, Cambridge, 2003.

[5] H. Zeisel, F. Durst, Computations of erosion-corrosion processes in separated two-phase flows, *NACE Corrosion,* NACE 1990 Paper no. 29.

[6] S. Zhou, M.M. Stack, R.C. Newman, Characterization of synergistic effects between erosion and corrosion in an aqueous environment using electrochemical techniques, *Corrosion*, **52** (1996) 934-946.

[7] M. Matsumura Erosion-corrosion of metallic materials in slurries, *Corros. Rev*., **12** (1994) 321-340.

[8] A. Neville T. Hodgkiess H. Xu An electrochemical and microstructural assessment of erosion-corrosion of cast iron, *Wear*, **235** (1999) 523-534

[9] W. Glaeser, I.G. Wright, Metals Handbook 9th Ed., *Corrosion*, **13** (1986), Ohio, ASTM Int'l. Metals Park

[10] J.P. Ault, Erosion corrosion of nickel aluminium bronze in flowing seawater, *NACE Corrosion*, 1995, Report No. 281.

[11] E.A. Culpan and G. Rose, Microstructural characterization of cast nickel aluminium bronze, *J. Mater. Sci*., **13** (1978) 1647-1657.

[12] P. Weill-Couly and D. Arnaud, *Fonderie*, **28** (1973) 123.

[13] E. Bardal, T.G. Eggen, T. Rogne, T. Solem, The erosion and corrosion properties of thermal spray and other coatings, Int. Thermal Spraying Conf., Kobe, Japan, 1995.

[14] M. Bjordal, E. Bardal, T. Rogne, T.G. Eggen, Erosion and corrosion properties of WC coatings and duplex stainless steel in sand-containing synthetic sea water, *Wear*, **186-187** (1995) 508-514.

[15] A.V. Levy, The erosion-corrosion behaviour of protective coatings, *Surf. Coat. Technol.*, **36** (1988) 387-406.

[16] B.Q. Wang, G.Q. Geng, A.V. Levy, Erosion-corrosion of thermal spray coatings, *Surf. Coat. Technol.*, **43-4** (1990) 859-874.

[17] J.M. Perry, A. Neville, V.A. Wilson, T. Hodgkiess, Assessment of the corrosion rates and mechanisms of a WC-Co-Cr HVOF coating in static and liquid-solid impingement saline environments, *Surf. Coat. Technol.*, **137** (2001) 43-51.

[18] K.S. Tan, Electrochemical analysis of the erosion-corrosion of HVOF aluminium bronze coatings, *PhD Thesis*, University of Southampton, 2003.

[19] F. Hasan, A. Jahanafrooz, G.W. Lorimer, N Ridley, The morphology, crystallography and chemistry of phases in as-cast nickel aluminium bronze, *Metall. Trans A*, **13A** (1982) 133-134.

[20] Y. Puget, K.R. Trethewey, R.J.K. Wood, Electrochemical noise analysis of polyurethane-coated steel subjected to erosion-corrosion, *Wear,* **233-235** (1999) 552-567.

[21] T. Hodgkiess, A. Neville, S. Shrestha, Electrochemical and mechanical interactions during erosion-corrosion of a high-velocity oxy-fuel coating and a stainless steel, *Wear*, **233-235** (1999) 623-634.

[22] J.B. Zu, I.M. Hutchings, G.T. Burstein, Design of a slurry erosion test rig, *Wear*, **140** (1990) 331-344.

[23] A.J. Moore, R.J.K. Wood, Erosive wear mapping in pipe materials, Plastic Pipes VIII, E1/4, Koningshof, Holland, Sept, 1992, 1-10.

[24] G.L Sheldon, I. Finnie, J.Eng. Ind. **88** (1966) 393.

[25] K.S. Tan, R.J.K. Wood, K.R. Stokes, The slurry erosion behaviour of High Velocity Oxy-Fuel (HVOF) sprayed aluminium bronze coatings, *Wear*, **255** (2003) 195-205.

[26] J.A. Hearley, J.A. Little, and A.J. Sturgeon, 'The erosion behaviour of NiAl intermetallic coatings produced by high velocity oxy-fuel thermal spraying', *Wear*, **233-235**, (1999), pp. 328-333.

[27] Wang, B. Q. and Lee, S. W., 'Erosion-corrosion behaviour of HVOF NiAl-Al2O3 intermetallic-ceramic coating', *Wear*, **239**, (2000), pp. 83-90.

[28] Mann, B. S. and Arya, Vivek, 'Abrasive and erosive wear characteristics of plasma nitriding and HVOF coatings: their application in hydro turbines', *Wear*, **249**, (2001), No. 5-6, pp. 354-360.

TABLES

Table 1: Chemical compositions of materials used in the current investigation.

P	S	Mn	Al	Ni	Fe	Cr	Mo	Si	C	Cu	Notes (mixing ratio)
		1.10	9	5	4.5	0.01	-	-	-	Bal	Cast NAB alloy
			8.71	5.55	4.50	1.02	0.15	0.06	0.01	Bal	HVOF NAB coating
			9.5		1.0					Bal	HVOF AB coating
0.05	0.05	1.6			Bal			0.5	0.25		BS 4360 steel

Table 2: Material Properties

	Cast NAB	HVOF NAB	HVOF AB	4360 Steel
Hardness(Vickers, HV_{100g}) [18]	235	290	300-330	149
Density (gcm^{-3})	7.64	7.69	7.64	7.87
As sprayed surface roughness (R_a, μm)	-	7 - 9	7 - 9	-
Surface roughness after polishing (R_a, μm)	-	0.01	0.01	-
As sprayed coating thickness (μm)	-	300	250	-

Table 3: Conditions used for the erosion and erosion-corrosion experiments

Experiments	Jet velocity (ms^{-1})	Sand diameter (μm)	Test solution	Flow rate ($kg\ min^{-1}$)	Impingement Angle	Sample size (mm)
Corrosion (C)	3.1-6	-	3.5 % NaCl	6.3-9.0	90°	40 × 40 × 5
Erosion (E)	3.1-6	135 and 235 (mean diameter)	3.5 % NaCl with CP	6.3-9.0	90°	40 × 40 × 5
Erosion-corrosion (T)	3.1-6	135 and 235 (mean diameter)	3.5 % NaCl	6.3-9.0	90°	40 × 40 × 5

Table 4: Mass loss measurements obtained for cast NAB, HVOF NAB coating and 4360 steel

Material/velocity	Mass loss (mg)					Percentages	
Steel	T	E	C	E+C	S	E/T %	S/T %
3.1 ms^{-1} (0.02 μJ)	12.20	14.10	12.30	26.40	-14.20	115.6	-117.0
3.1 ms^{-1} (0.09 μJ)	18.50	20.30	10.80	31.10	-12.60	109.7	-68.1
5.0 ms^{-1} (0.23 μJ)	27.50	27.50	11.70	39.20	-11.70	100.0	-42.5
6.7 ms^{-1} (0.41 μJ)	100.50	88.10	9.60	97.70	+2.80	87.7	+2.8
HVOF NAB	T	E	C	E+C	S	E/T %	S/T %
3.1 ms^{-1} (0.02 μJ)	3.80	3.00	2.40	5.40	-1.60	78.9	-42.2
3.1 ms^{-1} (0.09μJ)	4.90	4.60	2.50	7.10	-2.20	93.9	-44.9
5.0 ms^{-1} (0.23 μJ)	18.30	16.90	2.60	19.50	-1.20	92.3	-6.6
6.7 ms^{-1} (0.41 μJ)	49.10	39.70	3.90	43.60	+5.50	80.9	+11.2
Cast NAB	T	E	C	E+C	S	E/T %	S/T %
3.1 ms^{-1} (0.02 μJ)	3.30	2.86	1.53	4.39	-1.05	85.6	-31.4
5.0 ms^{-1} (0.04 μJ)	8.19	7.59	1.70	9.29	-1.10	92.6	-13.4
5.0 ms^{-1} (0.23 μJ)	12.10	10.47	1.70	12.17	-0.07	86.5	-0.57
6.0 ms^{-1} (0.33 μJ)	13.27	12.18	2.39	14.57	-1.30	91.7	-9.70

Table 5. Relationship between E_k and V_u for both erosion and erosion-corrosion of the HVOF coating and cast NAB

E_k (µJ)	Jet velocity (ms^{-1})	Sand diameter (µm)	V_{u_E} (μm^3/impact)	V_{u_T} (μm^3/impact)
HVOF NAB				
0.02	3.1	135	0.026	0.034
0.09	3.1	235	0.215	0.229
0.23	5.0	235	0.663	0.720
0.41	6.0	235	1.201	1.486
Cast NAB				
0.02	3.1	135	0.015	0.026
0.04	5.0	135	0.041	0.046
0.23	5.0	235	0.297	0.344
0.33	6.0	235	0.277	0.301

Table 6. Comparison of the E_k exponents (l) under erosion and erosion-corrosion conditions

Material	E_k exponent for E	E_k exponent for T
Cast NAB	1.03	0.93
HVOF AB	1.47	-
HVOF NAB	1.21	1.18
4360 steel	0.79	0.87

Table 7. Potential particle kinetic energies for marine components

	Marine component			
	Pipe	**Valve**	**Pump**	**Propulsor**
Velocity (ms^{-1})	0 - 3	5	10	25
Particle diameter (μm)	100	100	100	100
Particle kinetic energy (μJ)	0 - 0.007	0.02	0.07	0.44

FIGURES

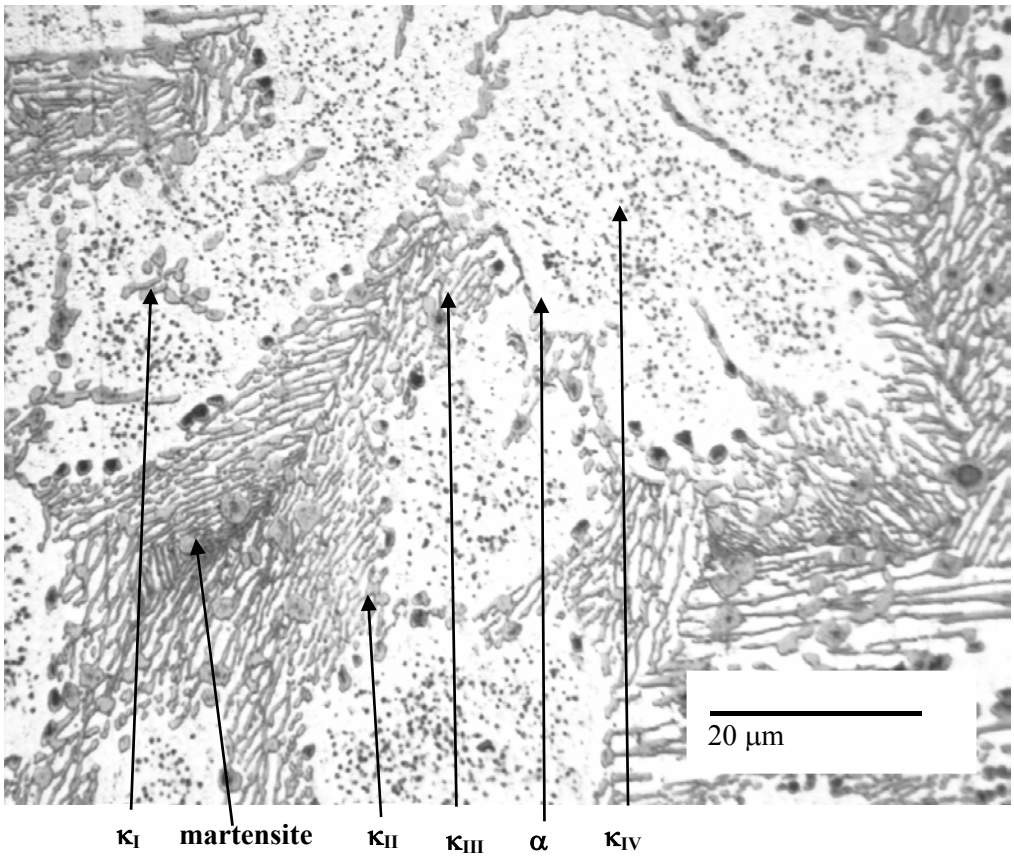

Figure 1: Microstructure of cast NAB after etching with 10%wt. $FeCl_3$ in methanol.

a)

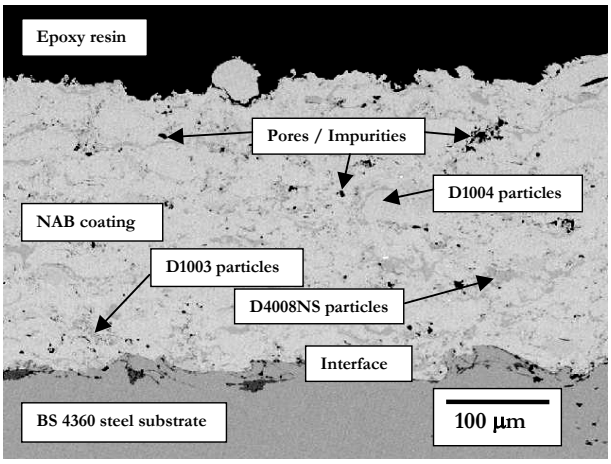

b)

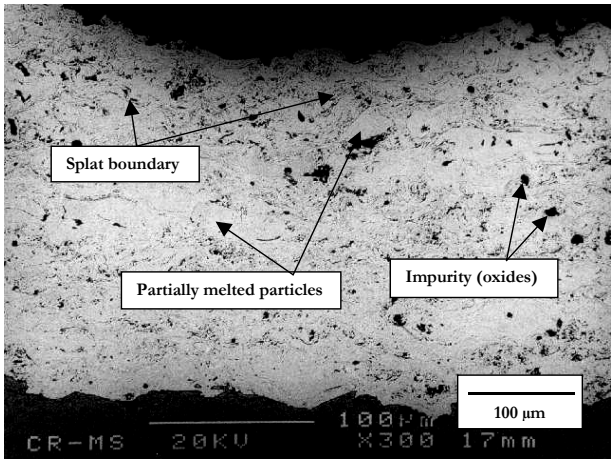

Figure 2: SEM of (a) HVOF NAB and (b) HVOF AB coating transverse sections showing coating morphology, particles/splats and impurities within the coatings.

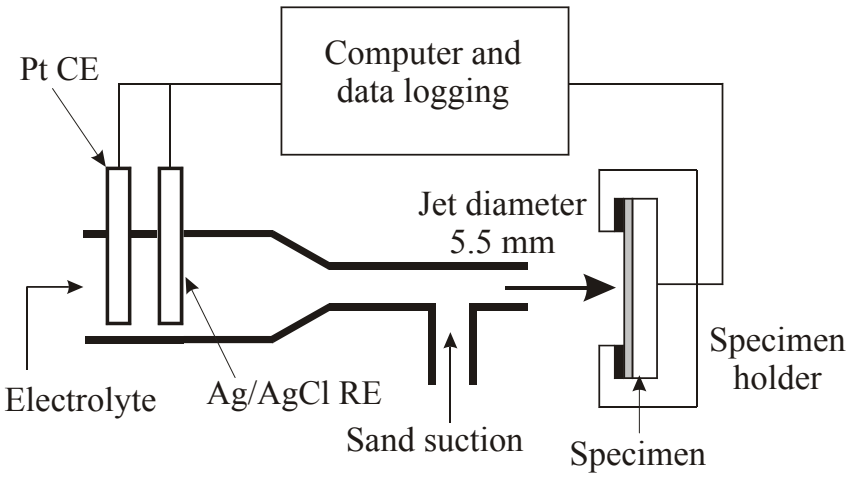

Figure 3: The low kinetic energy rig instrumented to made electrochemical measurements.

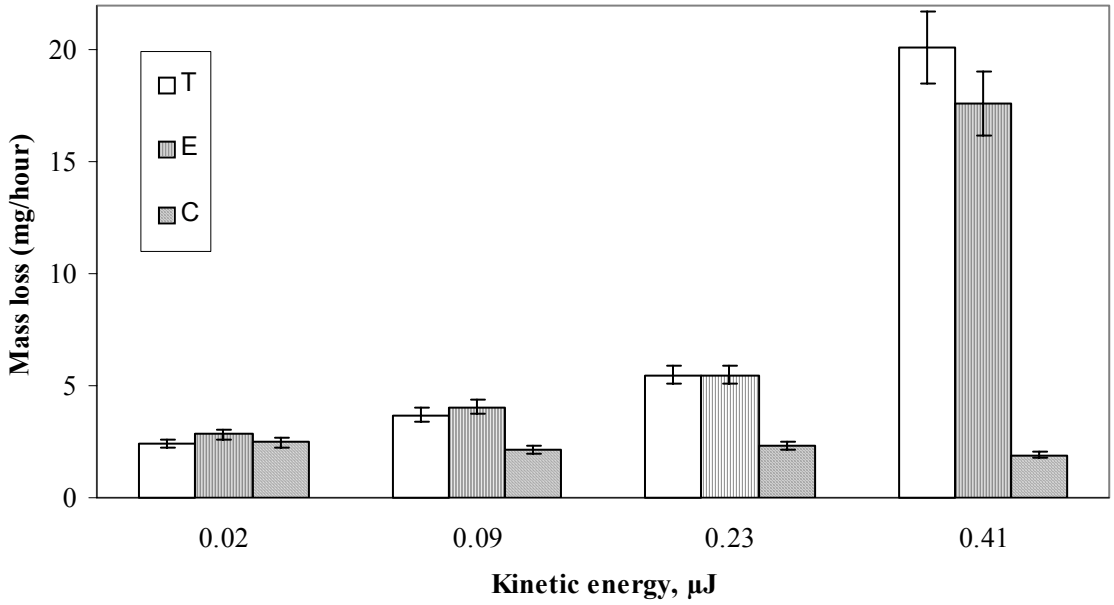

Figure 4: Mass loss rates for 4360 steel at different kinetic energies. Conditions: 3.0 % w/w silica sand concentration, 3.5 % NaCl solution.

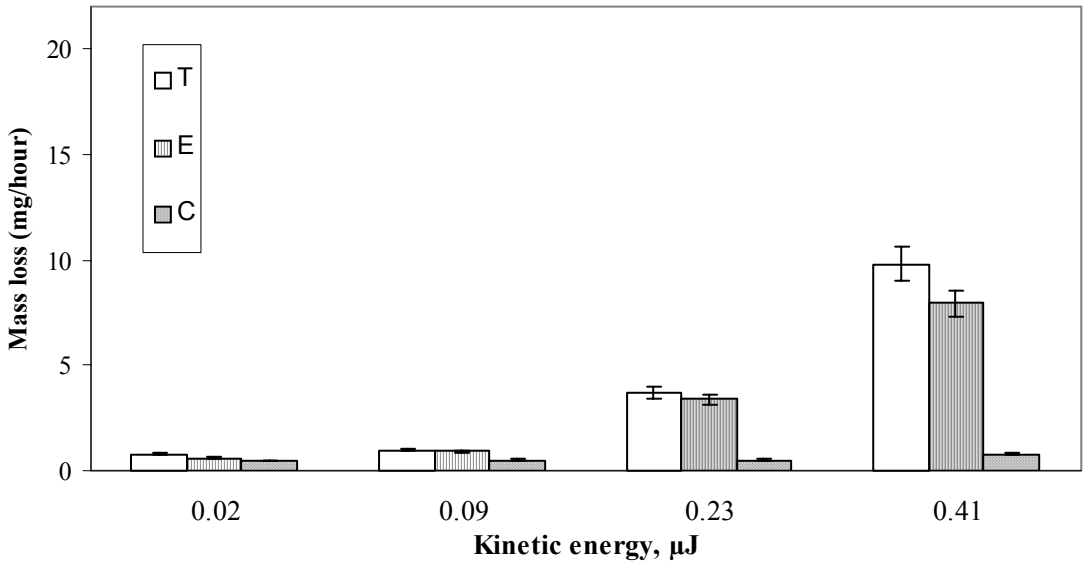

Figure 5: Mass loss rates for HVOF NAB coating at different kinetic energies. Conditions: 3.0 % w/w silica sand concentration, 3.5 % NaCl solution.

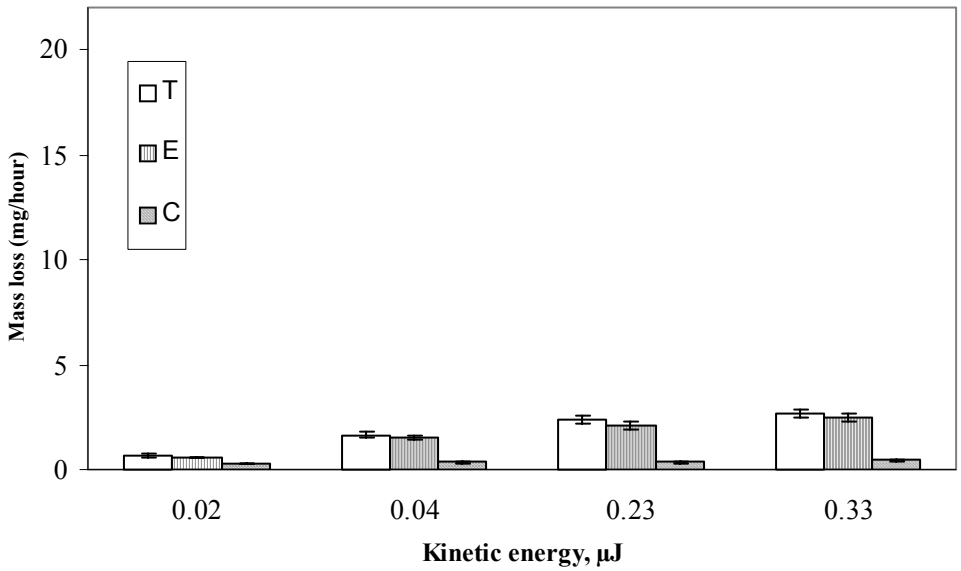

Figure 6: Mass loss rates for cast NAB at different kinetic energies. Conditions: 2.5-3.0 % w/w silica sand concentration, 3.5 % NaCl solution.

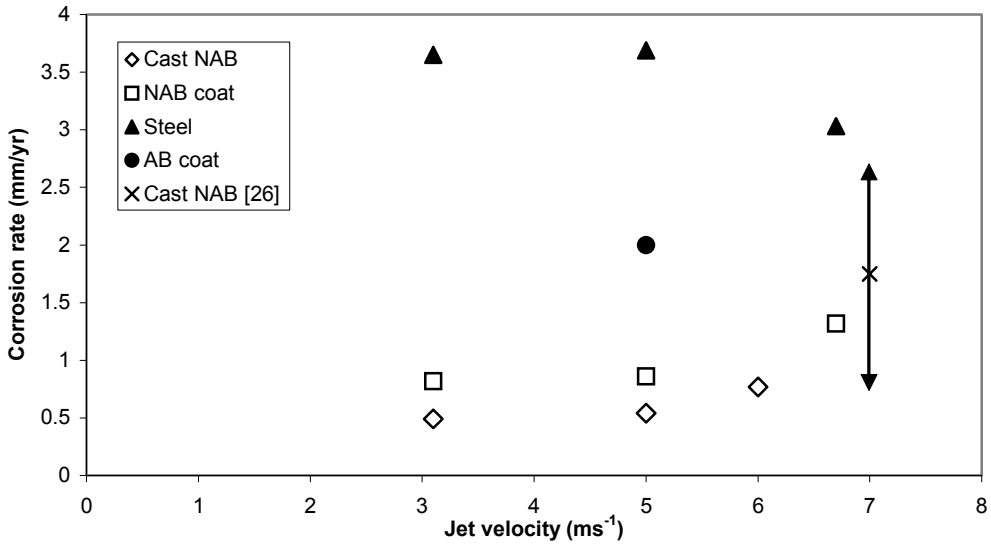

Figure 7: Comparison of flow corrosion rates for cast NAB, NAB coating, steel, and AB coating at various jet velocities.

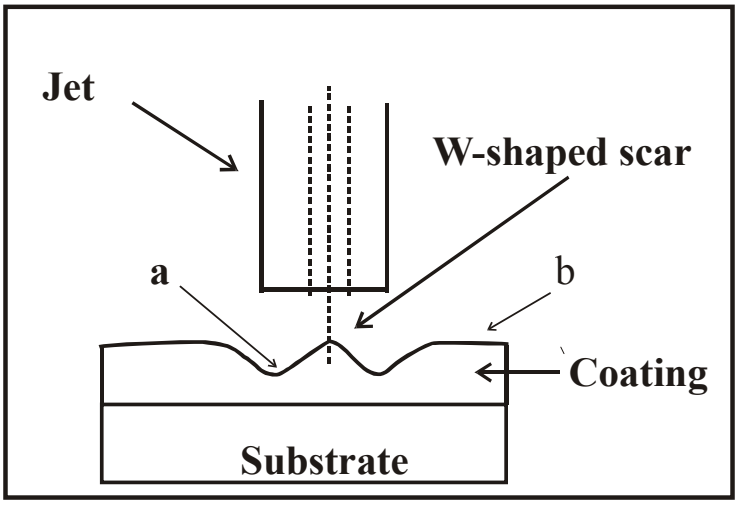

Figure 8: Schematic diagram of erosion-corrosion samples showing the scar where SEM was carried out: (a) at the location of maximum erosion depth within the scar and (b) outside the scar region.

a) **b)**

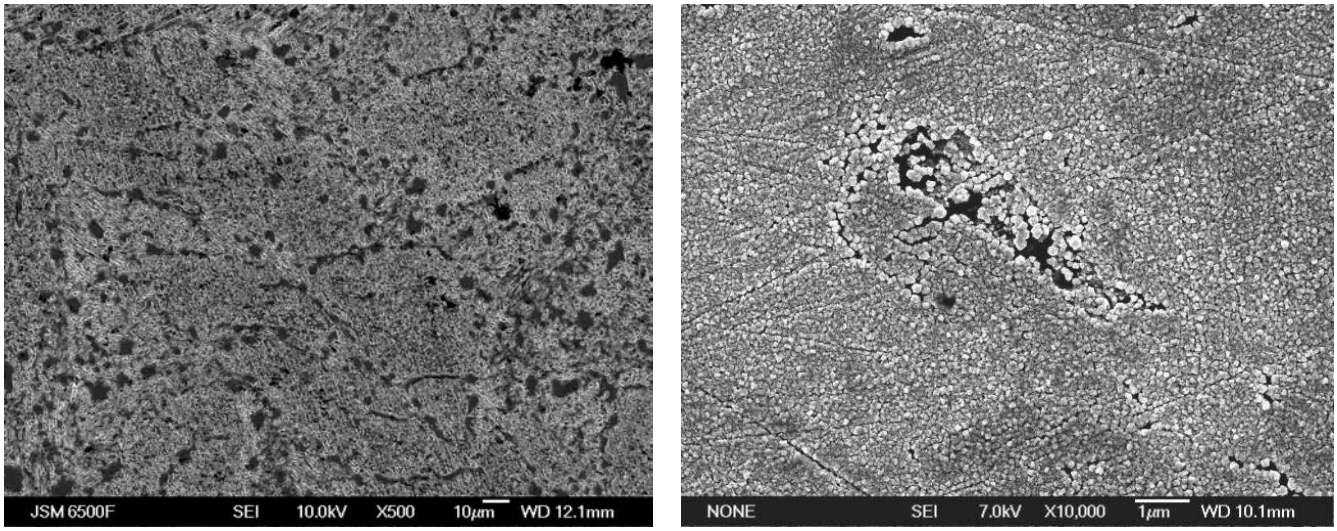

Figure 9: SEM micrograph of (a) cast NAB and (b) HVOF NAB coating flow corrosion surface showing clear evidence of selective phase corrosion. Conditions: 3.5% NaCl, 3.1 ms^{-1} after 5 hours.

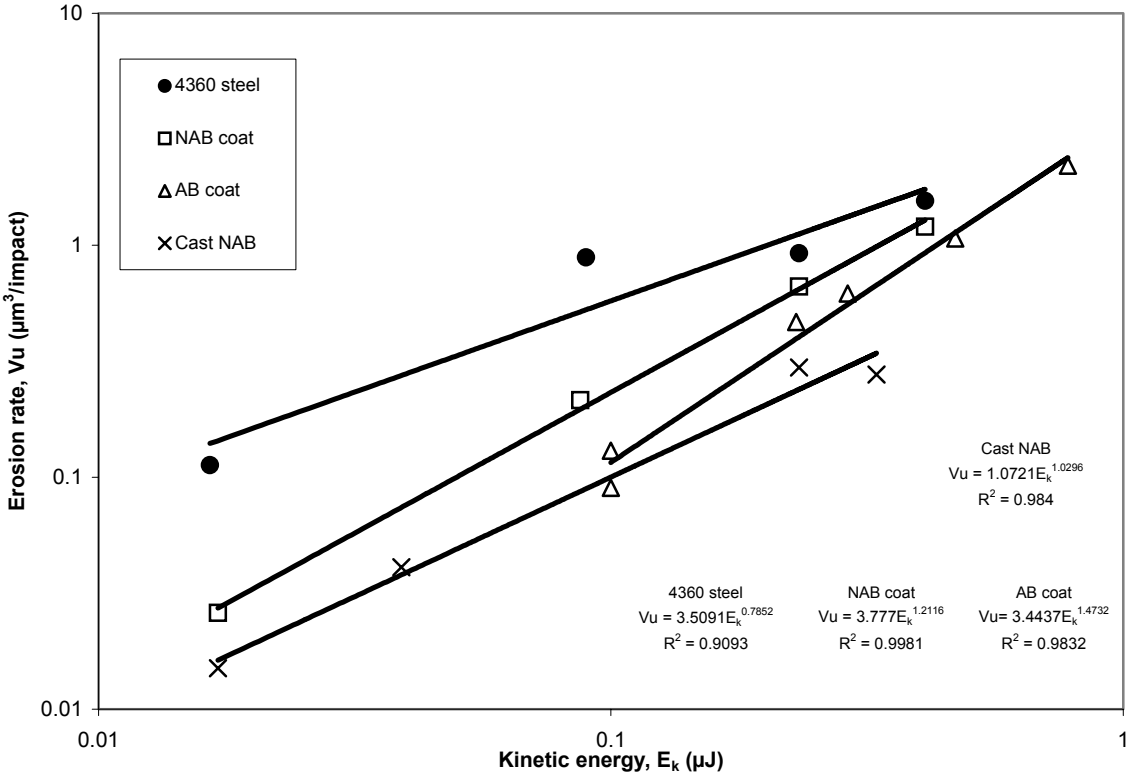

Figure 10: Relationship between erosion rate and kinetic energy for cast NAB, NAB coating, AB coating and 4360 steel.

a) Cast NAB

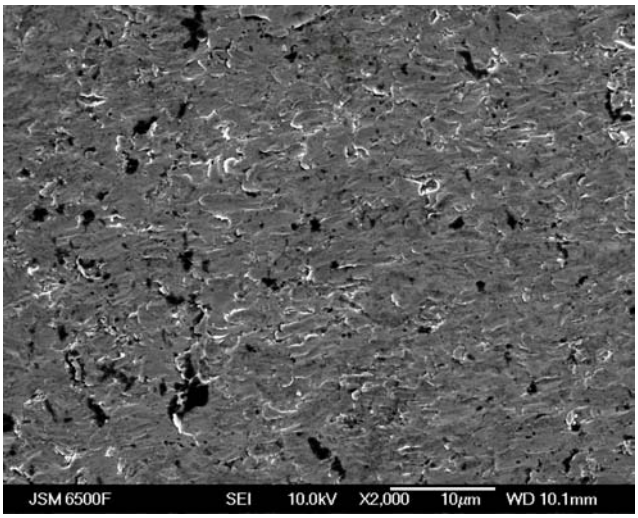

b) Cast NAB

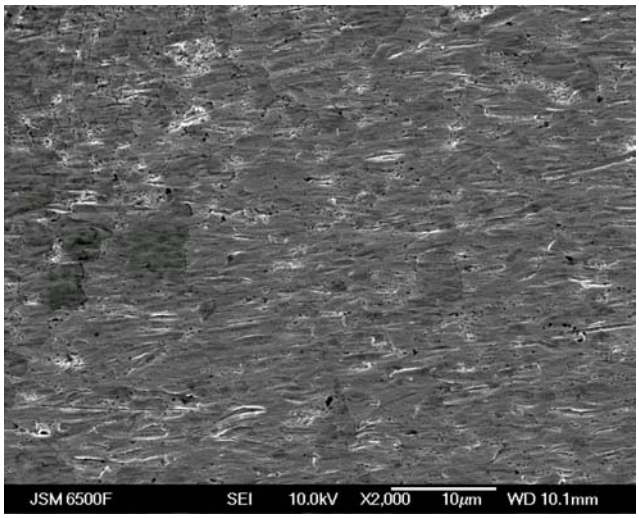

c) HVOF NAB

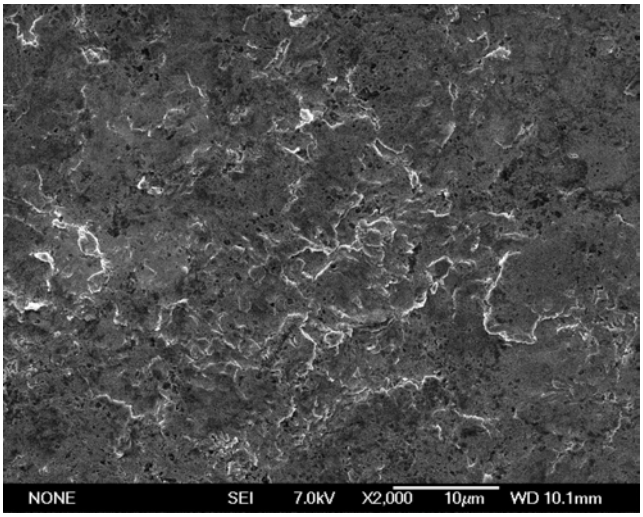

d) HVOF NAB

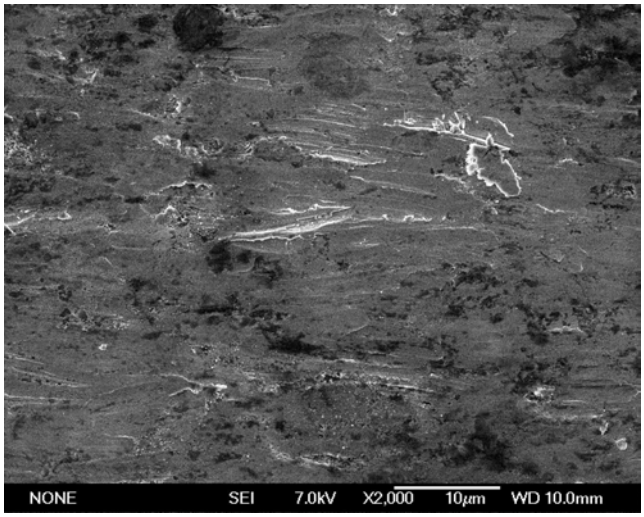

Figure 11: SEM micrographs of cast NAB and HVOF NAB coating erosion surfaces at the location of maximum erosion depth within the scar (a) and (c) respectively, and (b) and (d) the edge of the wear scar. Conditions: 3.0 % w/w silica sand concentration, 3.5% NaCl, 3.1 ms-1 after 5 hours.

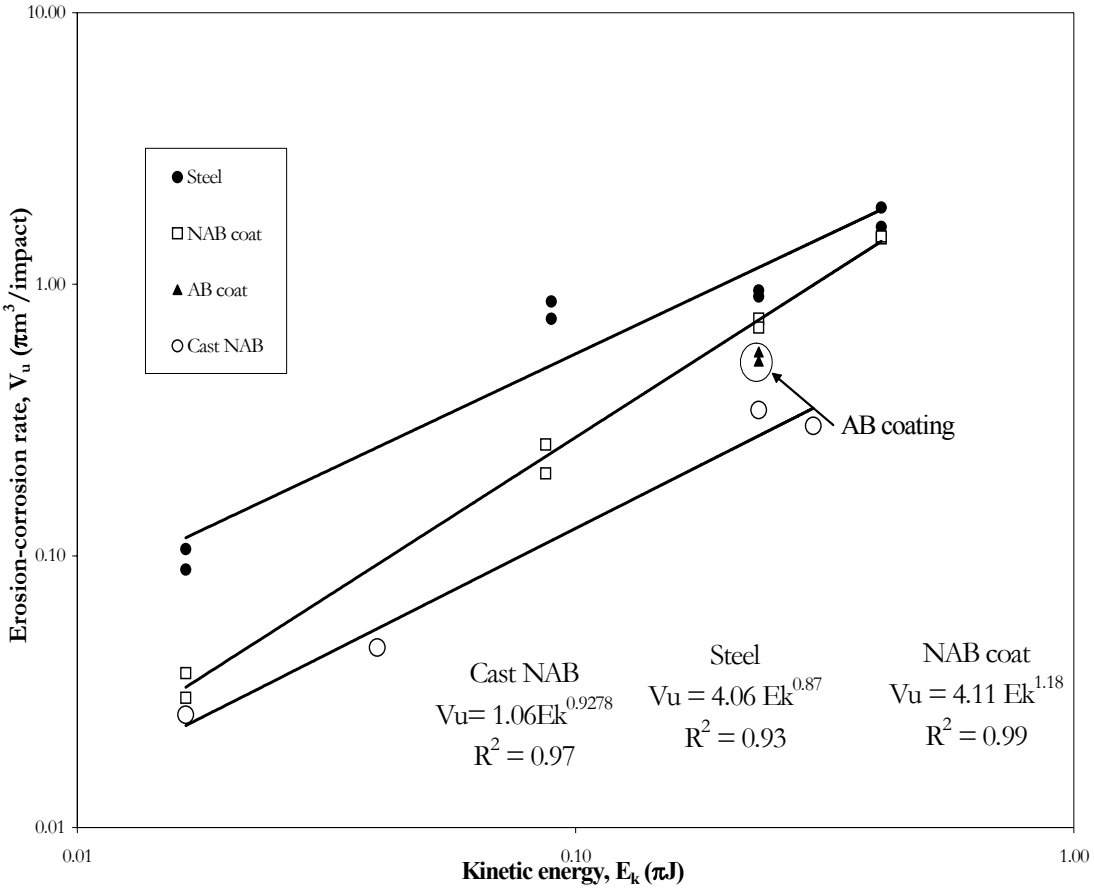

Figure 12: Relationship between erosion-corrosion rate and kinetic energy.

a) Cast NAB

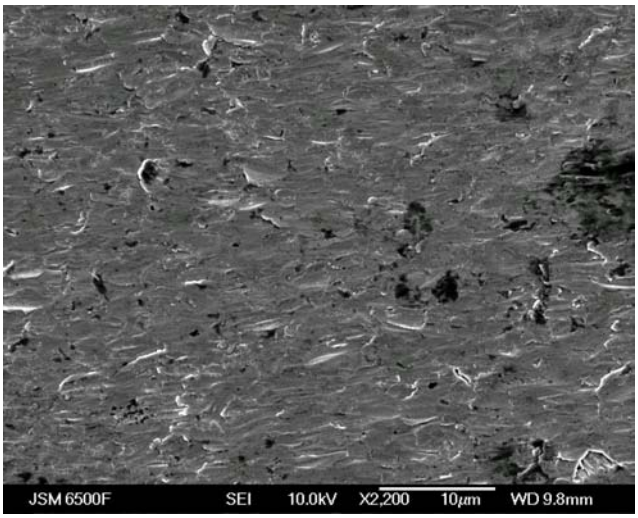

b) Cast NAB

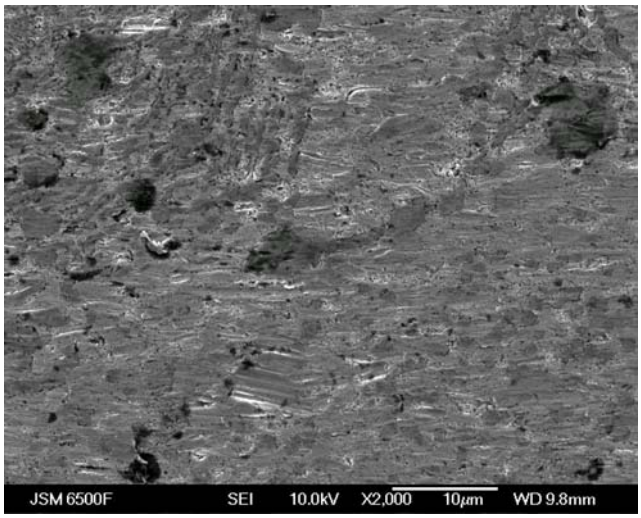

c) HVOF NAB

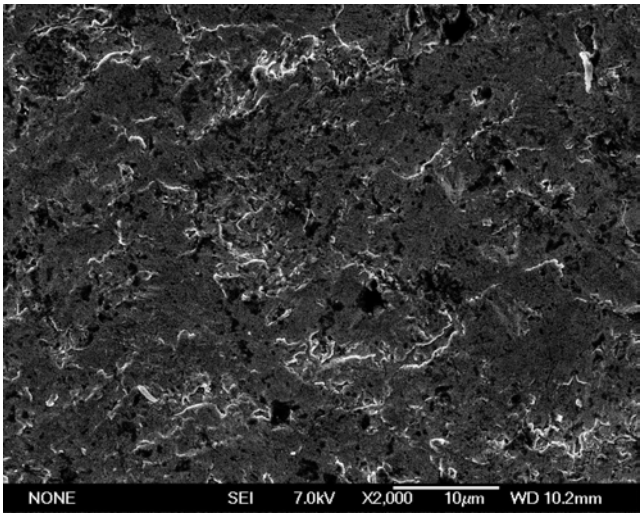

d) HVOF NAB

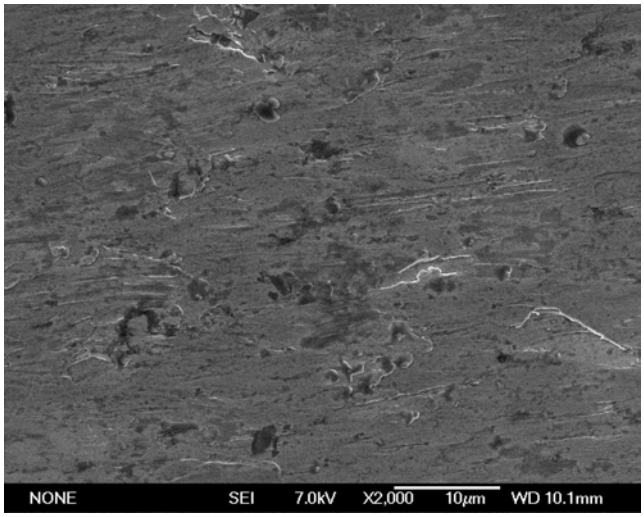

Figure 13: SEM micrographs of cast NAB and HVOF NAB coating erosion-corrosion surfaces at the location of maximum erosion depth within the scar (a) and (c) respectively, and (b) and (d) edge of the wear scar. Conditions: 3.0 % w/w silica sand concentration, 3.5% NaCl, 3.1 ms-1 after 5 hours.

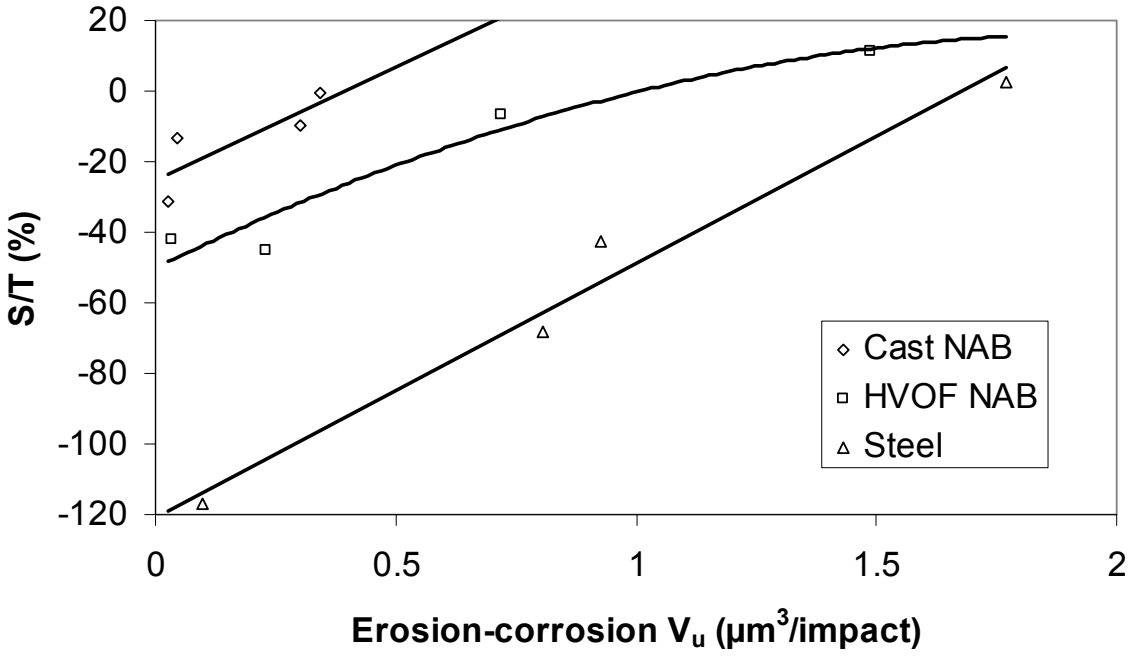

Figure 14: Relationship of synergy percentage with V_{u_T} .